SAND2021-9213R

FY21 Status Report: Probabilistic SCC Model for SNF Dry Storage Canisters

Spent Fuel and Waste Disposition

Prepared for
U.S. Department of Energy
Spent Fuel and Waste Science and Technology

Nathan W. Porter, Dusty Brooks,
Charles Bryan, Ryan Katona,
and Rebecca Schaller
Sandia National Laboratories

July 30, 2021
M3SF-21SN010207057
SAND21-XXXXX

Sandia National Laboratories is a multimission laboratory managed and operated by National Technology & Engineering Solutions of Sandia, LLC, a wholly owned subsidiary of Honeywell International Inc., for the U.S. Department of Energy's National Nuclear Security Administration under contract DE-NA0003525.

Prepared by
Sandia National Laboratories
Albuquerque, New Mexico 87185 and Livermore, California 94550

Sandia National Laboratories is a multimission laboratory managed and operated by National Technology and Engineering Solutions of Sandia, LLC, a wholly owned subsidiary of Honeywell International, Inc., for the U.S. Department of Energy's National Nuclear Security Administration under contract DE-NA0003525.

U.S. DEPARTMENT OF ENERGY

Sandia National Laboratories

NNSA National Nuclear Security Administration

SUMMARY

Stress corrosion cracking (SCC) is an important failure degradation mechanism for storage of spent nuclear fuel. Since 2014, Sandia National Laboratories has been developing a probabilistic methodology for predicting SCC. The model is intended to provide qualitative assessment of data needs, model sensitivities, and future model development. In fiscal year 2021, improvement of the SCC model focused on the salt deposition, maximum pit size, and crack growth rate models.

- Parameterization of the previous salt deposition model presented significant challenges. Measured salt deposition data are sparse with high uncertainties, and the model results are very sensitive to parameter and modeling changes. Instead, a distribution is proposed that samples salt deposition directly based on a range informed by operational data. In general, the new approach results in smaller salt deposition rates and should lead to smaller pit size predictions.
- The maximum pit size model was modified to incorporate experimental data that has only recently become available, which enables the model to better characterize the important electrochemical kinetics relevant to this phenomenon. For any given environmental condition, the new model generally predicts larger maximum pit sizes compared to the old model.
- Lastly, the crack growth rate model was re-calibrated, and the implementation was modified to resolve a code bug. Calibration of the crack growth rate model was performed using a frequentist linear regression approach similar to previous calibration efforts, but the data set used for calibration was substantially expanded to include data from experiments in which specimens were immersed for the duration of the experiment. The previous calibration had only used data collected under atmospheric conditions, which was both limited and less accurate. Though the new calibration results in only a small change to the previous model, the wider range of experimental data lends more justification to the resulting distributions.

All three updates constitute major changes to the modeling approach and will have an impact on predicted SCC quantities of interest; however, the overall effect remains a topic for future study. Currently, the changes to the salt deposition and maximum pit size models have opposing effects on maximum pit size predictions. Since changes to the maximum pit size will impact the timing of crack initiation, these model changes may have drastic effects on the overall model predictions. Though the crack growth rate model has been re-calibrated and the model has more experimental justification, the new parameter distributions are not expected to have a significant impact on the code predictions.

This page is intentionally left blank.

CONTENTS

LIST OF FIGURES

LIST OF TABLES

This page is intentionally left blank

ACRONYMS

CFD	computational fluid dynamics
CFR	Code of Federal Regulations
CGR	crack growth rate
DSC	dry storage canister
EPRI	Electric Power Research Institute
ISFSI	independent spent fuel storage installation
MSE	mean squared error
NRC	U.S. Nuclear Regulatory Commission
PNNL	Pacific Northwest National Laboratory
SCC	stress corrosion cracking
SNF	spent nuclear fuel
SNL	Sandia National Laboratories

This page is intentionally left blank.

SPENT FUEL AND WASTE SCIENCE AND TECHNOLOGY

FY21 STATUS REPORT: PROBABILISTIC SCC MODEL FOR SNF DRY STORAGE CANISTERS

1. INTRODUCTION

Spent Nuclear Fuel (SNF) is initially stored at nuclear power reactor sites in spent fuel pools for at least one year. After sufficient cooling and radioactive decay, SNF is loaded into sealed casks or welded canisters filled with inert gas. Some casks are self-shielding, but the welded canisters are placed within passively-ventilated concrete or concrete/steel overpacks, which serve as radiation shielding; the canister and overpack together represent the dry storage system. The waste is stored at reactor sites in Independent Spent Fuel Storage Installations (ISFSIs). To date, there are more than 3000 dry storage canisters (DSCs) stored at over 70 ISFSIs in the United States [1].

The current regulatory framework for ISFSIs is governed by the U.S. Nuclear Regulatory Commission (NRC) and documented primarily in 10 CFR Part 71 [2] and 10 CFR Part 72 [3]. Additional documentation can also be found in various NRC Regulatory Guides [4, 5], NUREG reports [6, 7], NUREG/CR reports [8, 9], and NRC Staff Guidance [10, 11, 12]. The current regulatory framework allows for an initial 40-year licensing term, followed by a license renewal for a term of up to 40 years.

Since a repository for SNF disposal is unlikely, the DSCs will remain at ISFSIs or at a future centralized storage facility for the foreseeable future. For the existing regulatory period of 80 years, design and performance of DSCs has been extensively studied and the effectiveness of existing regulations has been demonstrated through significant operational experience. However, compliance with existing regulatory frameworks has not been established beyond the current 80-year licensing period. Because SNF remains significantly radioactive for tens to hundreds of thousands of years [13], extending the regulatory guidance will become increasingly important over the next few decades.

A phenomenon that is of particular concern for degradation analysis of DSCs is stress corrosion cracking (SCC), which is sometimes referred to as atmospheric stress corrosion cracking (ASCC) or chloride-induced stress corrosion cracking (CISCC). An illustration of this process and the necessary models is shown in Figure 1-1. Atmospheric SCC describes the buildup of salt aerosols on the surface of a metal that will deliquesce to form a corrosive brine, the formation and growth of small pits, the nucleation of cracking at the pit sites, and the propagation of the crack through the material thickness. SCC is an important mode of failure because crack penetration through the canister can initiate a release of radioactive material. Modeling of SCC requires complex models for weather, salt deposition, pit size, stresses, pit-to-crack transition, and crack growth.

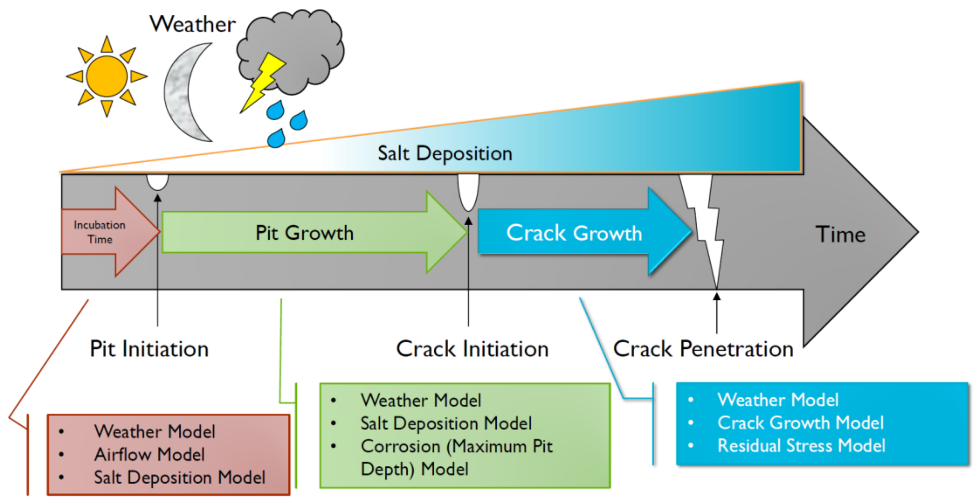

Figure 1-1. Illustration of the transient SCC process and corresponding models

Three criteria must be met for SCC to take place: (1) the metal of interest must be susceptible, (2) a corrosive environment must exist (in this case, through deliquescence of deposited salt aerosols), and (3) there must be sufficient tensile stress in the material. It is well-documented that austenitic stainless steels, including those that are used in DSCs, can undergo SCC [14]. Both modeling [16] and experimental measurements [17] have shown that through-wall tensile stresses are likely present in canister welds. Finally, numerous field studies have shown that chloride-rich salt aerosols are deposited on the canister surfaces; these aerosols will eventually deliquesce to produce potentially corrosive brines [18], [19], [20], [21]. For these reasons, understanding the timing and occurrence of canister SCC continues to be an important technical gap for the back end of the nuclear fuel cycle [22].

Sandia National Laboratories (SNL) leads a multi-lab DOE effort to understand the timing, occurrence, and consequence of potential canister SCC, and as part of that effort, has developed a probabilistic model for canister penetration by SCC. This model has been developed and continuously updated at SNL since 2014 [23, 24, 25, 26]. Model uncertainties are treated using a nested loop structure, where the outer epistemic loop accounts for uncertainties due to lack of data and the inner aleatoric loop accounts for uncertainties due to natural variation in nature. By separating uncertainties into these categories, it is possible to focus future work on reducing the most influential epistemic uncertainties. Several experimental studies have already been performed to improve the modeling approach through expanded process understanding and improved model parameterization [27]. The resulting code is physics-based and intended to inform work which identifies (1) important modeling assumptions, (2) experimental data needs, and (3) necessary model developments. In this document, three updates are described to the modeling approach.

1. The salt deposition model is difficult to parameterize; therefore, it has been replaced by a constant salt deposition rate with bounded uncertainty (see Section 2). This approach is less flexible and does not incorporate site-specific knowledge of canister salt loads. The parameterization will be replaced once a validated salt deposition model has been developed, but until then, it allows parametric studies.
2. In Section 3, the pit size model has been updated to be consistent with new experimental data.
3. The model for calculating crack growth rates in stainless steel was previously only calibrated using experimental data for atmospheric corrosion [28]. In Section 4, the model has been updated to include immersed corrosion data from a variety of sources in the literature. Immersed SCC crack growth rate data are collected using well-established methods and are commonly more accurate than data collected under atmospheric conditions. Only recently has confidence risen

that the same mechanism controls crack growth rate under both sets of conditions, allowing use of the immersed data in the canister SCC model.

2. SALT DEPOSITION

In the environments of concern for DSCs, the corrosive agent is primarily chloride salt aerosols that originate from three sources: the ocean, road salts, and cooling towers. The amount of salt deposited on the surface of a canister controls the thickness of the brine layer formed by salt deliquescence, which is an influential parameter in determining the maximum pit size that can occur, a controlling factor for initiation of a SCC crack. Deposition rates are highly variable, but proximity to an ocean is a primary factor. This is shown in Figure 2-1, which plots ground deposition rates at various sites around the world as a function of distance from the nearest ocean[a]. There is a clear logarithmic trend, indicating that salts from ocean sources are a dominant factor.

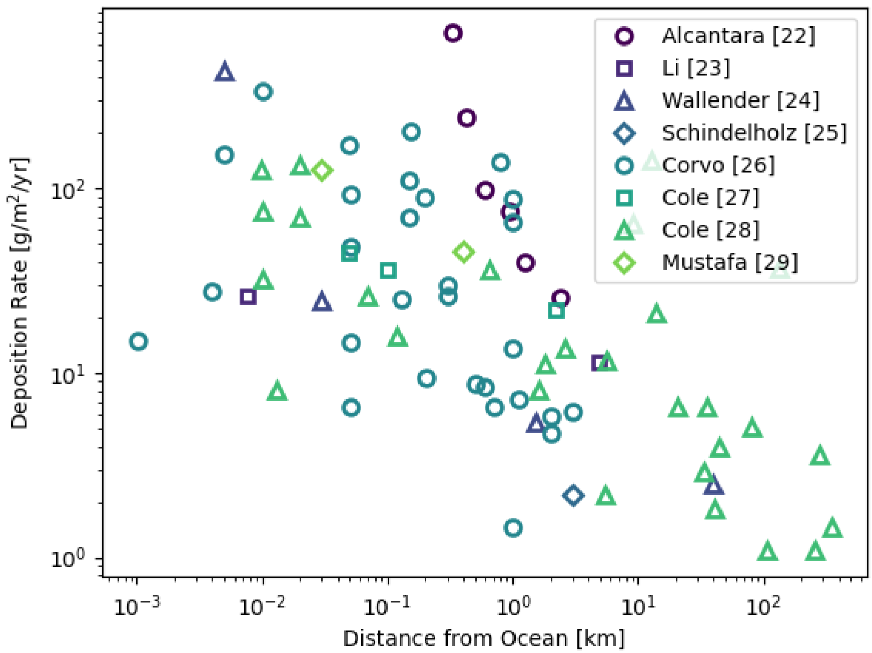

Figure 2-1. Experimentally measured deposition rates (reproduced from [26])

Though salt deposition rates should clearly be correlated to distance from an ocean, other aspects of the previous modeling approach [26] for salt deposition rates are difficult to parameterize. Overall, there is a lack of experimental data and large variation between different ISFSI sites. The model is very sensitive to parameterization of the deposition velocity model [37], the linear fowling model [38], fluid property calculations, surface friction, as well as the particle size distributions for each source of salt. Since all these models are difficult to parameterize, the resulting deposition densities are highly uncertain and unreliable.

In fact, similar studies for modeling salt deposition have had similar modeling challenges. Work at PNNL has developed a Computational Fluid Dynamics (CFD) informed model using STAR-CCM+ simulations [39]. The resulting model is highly sensitive to the physical processes that are incorporated (e.g., thermophoresis, turbophoresis, etc.), and the resulting deposition rates were not compared to

[a] The deposition rates in Figure 2-1 are measured in open air, not on DSCs. Deposition velocities on the surface of a DSC will be much lower than in open air, resulting in lower deposition rates. However, the deposition rates on both types of surface are dependent upon the quantity of available salt aerosols and should therefore have a similar logarithmic relationship with proximity to an ocean.

experimental results, because no relevant data were available. Similar to the approach taken at SNL [26], the Electrical Power Research Institute (EPRI) developed a deposition model using linear fouling [38]. Through comparison of simulation results to measured deposition rates at ISFSIs, they concluded that the model results were only within about an order of magnitude of the field data and that the model was conservative.

An accurate and predictive model for salt deposition rates has not yet been proposed in the literature. Therefore, the current approach is modified to parameterize the salt deposition rate based on operational data at real sites. Here, we utilize operational data obtained from various sites, as shown in Table 1 [38]. A realistic model for the chloride deposition rate would be a function of distance from the ocean and location on the canister. However, the data in Table 1 has few data points and large uncertainties, which would impart large errors on any attempt at characterization of the functional form for deposition rate. Therefore, the salt deposition rate is given the log-uniform distribution $\mathrm{logU}(10^{-4}, 0.5)$, which is equivalent to a uniform distribution in log space. The chosen distribution is shown in Figure 2-2. This parameterization will (1) incorporate all available data for characterization of deposition rates, (2) be site-independent, and (3) allow chloride deposition rate to be varied for sensitivity studies.

Table 1. Measured average chloride accumulation rates at different sites (reproduced from [38])

Case	Chloride [g/m²/yr]	
	Top surface	Vertical surface
Fukushima	$0.3 - 0.5$	$0.02 - 0.1$
Tokai	-	< 0.001
Diablo Canyon	-	< 0.0025
Hope Creek	$0.001 - 0.01$	< 0.0015
Main Yankee	< 0.0004	0.0001
Calvert Cliffs	$0.0001 - 0.004$	-

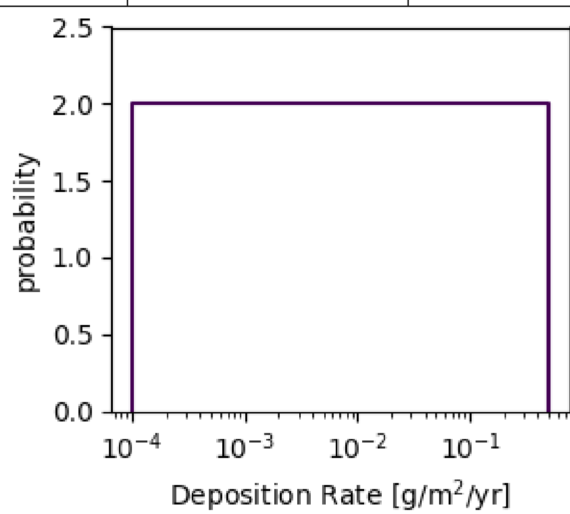

Figure 2-2. Probability density function for chloride deposition rate

In the SCC code, a new log-uniform distribution has been added so that chloride deposition rate can be sampled for each aleatory loop. By removing the complex calculation of deposition rate at each time step and weld location, the simulation time is reduced by about 95% (from about 100 seconds to 5 seconds per 100-year transient). This reduction in run time is ideal for probabilistic analysis, as it enables many query problems such as sensitivity and uncertainty analysis.

Note that this implementation *does not capture* site-specific variations in the salt deposition rate. These variations have been observed and are due to differences in surface orientation, salt aerosol quantities, and particle size distributions. To some extent, these variations could be incorporated into the parameterization in the future by incorporating measured salt concentrations for more accurate prediction at a given site.

3. MAXIMUM PIT SIZE

Once deposited salts deliquesce on a susceptible metal surface, corrosion can occur, and pits can form. The pits eventually grow large enough to serve as nucleation sites for the stress-driven cracks characteristic of SCC. Therefore, estimation of pit formation, growth, and pit-to-crack transition is an important step in the probabilistic modeling of SCC. Consistent with previous analyses [26], the conservative assumption is made that pit nucleation is not a limiting factor in pit formation. Rather, pits nucleate instantaneously once the relative humidity is greater than an experimentally determined threshold relative humidity [40].

Once pits form, they are assumed to be hemispherical and electrochemical kinetics are used to calculate the radius. A schematic is shown in Figure 3-1, where the anode (pit) and the coupled cathode, which supplies current to the anode, is on the metal surface around the pit. For any given pit, the cathodic current I_c available to support pit growth must exceed the anodic current I_a demand. If sufficient cathodic supply is not available to support dissolution, a pit will repassivate. Since I_a increases monotonically with pit size, matching of I_a and I_c is used to determine the maximum possible pit size given any local conditions. Consistent with previous work, the model of Chen et al. [41] [42] is used to approximate the maximum pit size.

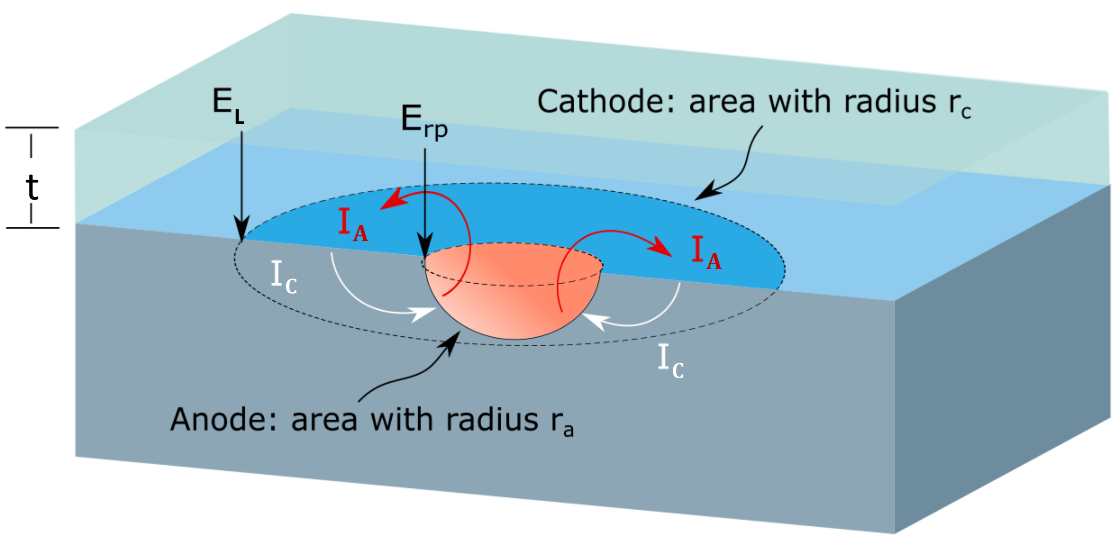

Figure 3-1. Schematic of a pit and the corresponding cathode

In the Chen model, the maximum cathodic current $I_{c,max}$ is expressed as

$$\ln I_{c,max} = \left[\frac{4\pi\kappa t \Delta E_{max}}{I_{c,max}} + \ln\left(\pi e r_a^2 i_{eq}\right)\right], \tag{3.1}$$

Where κ is the brine conductivity, t is the brine thickness, $\Delta E_{max} = E_L - E_{rp}$ is the potential drop from the pit edge to the outer cathode edge, e is Euler's number, r_a is the anode (pit) radius, and i_{eq} is the maximum equivalent current density for the cathode. The brine properties are determined from the property tables in [43] using the canister temperature and weather models as described in [26], the pit radius is the quantity to be solved for, and the remaining quantities are parameterized in the model.

Once the maximum cathodic current can be calculated, the anode current must also be determined. This value is called the pit stability criterion (measured in one dimension) and expressed as I_a/r_a for a hemisphere. The following sections document the parameterization of ΔE_{max}, i_{eq}, and I_a/r_a in the previous and new models.

3.1 Previous Model Parameterization

In the previous model implementation, the maximum cathode equivalent current density i_{eq} was calculated as the average current available over the cathode as

$$i_{eq} = \frac{\int_{E_L}^{E_{rp}} \left(i_c(E) - i_p\right) dE}{E_L - E_{rp}}, \tag{3.2}$$

Where the integration is between the potentials at the cathode edge E_L (open circuit potential) and the anode edge E_{rp} (repassivation potential), $i_c(E)$ is the cathodic current density function, and i_p is the passive current density at the anode edge. The repassivation potential E_{rp} is calculated based on [44] and $E_L = -0.2$. Equation (3.2) is integrated analytically using the following functional form of $i_c(E)$:

$$i_c(E) = i_p 10^{\frac{E-E_L}{b}}, \tag{3.3}$$

Where $b = U(-0.138, -0.169)$ is estimated based on experimental data [45]. The passive current density is approximated using the same equation evaluated at reference repassivation conditions.

$$i_p = i_{rp,\,ref} 10^{-\frac{E_{rp,ref}-E_L}{b}} \tag{3.4}$$

The remaining parameters ($i_{rp,ref}$ and $E_{rp,ref}$) are given values from [45]; see [26] for details. Finally, the pit stability criterion is bounded using a normal distribution based on bounds suggested in [42]: $I_a/r_a = U(1, 3)$.

Though the above modeling approach incorporates the state of knowledge at the time it was incorporated, it is highly uncertain. The experimental data used to evaluate the integral in Equation (3.2) can exhibit time-dependent effects and large fluctuations in parameters. The experimental basis [45] is derived from experiments at a single temperature (25°C) for NaCl brines on 304 stainless steel. Therefore, variations with temperature or chloride species are not treated. This is especially important for DSCs because elevated temperatures are expected on the metal surface and other chloride species are expected to be present in the brine. Therefore, additional experimental data was required to better inform the model for elevated temperatures, ranges of relative humidity, and brine composition.

3.2 New Model Parameterization

It is not necessary to implement an analytical integration to calculate equivalent anodic current density, since Equation (3.1) is only a function of ΔE_{max} and i_{eq}. Therefore, the new model calculates i_{eq} from a fit to experimental data [46]. A constant value is used for ΔE_{max} ($0.18\ V$), which is consistent with the experimental values that showed very little variation.

To experimentally determine i_{eq}, a polarization scan and determination of E_{rp} is necessary. Polarization scans were measured in a chloride-free solution to prevent convolution of cathodic kinetics with anodic dissolution due to open circuit localized corrosion. To determine the composition of the surrogate chloride-free solution, the product of $D_{O_2}C_{O_2}$, where D_{O_2} is the diffusivity of oxygen and C_{O_2} is the concentration of oxygen, was matched between the chloride solution and the non-chloride solution. The applicability of this method has been shown in multiple studies [47, 48, 46]. Polarization scans were determined in multiple surrogate solutions as a function of RH and temperature.

In addition to the polarization scan, 1D electrodes were utilized in order to determine $(i \cdot x)_{sf}$ and E_{rp} using the method of Srinivasan and Kelly [49]. A SS304L wire with a diameter of 50 µm was embedded in epoxy so that the diameter of the wire was exposed. Samples were subsequently placed in a temperature controlled (±0.1 ˚C) electrochemical cell with the chloride solution of interest and an anodic potential of +0.75 V_{SCE} was applied for 5 to 20 minutes. The potential was stepped down to +0.45 V_{SCE} for different time periods to allow for pit propagation to different depths. A polarization scan from +0.45 V_{SCE} to -0.6 V_{SCE} at a scan rate of 5 mV/sec was performed. After the polarization scan, the pit was immediately reinitiated by polarization to +0.75 V_{SCE}, and the cycle was repeated. Eight to ten repetitions of the cycle were performed as it has been shown that the pit depth needs to exceed 8-10 times the diameter (~400-500 µm) to prevent measured values from being influenced by the hemispherical diffusion at the pit mouth. Faraday's law and Fick's first law were then used to determine $(i \cdot x)_{sf}$. Using the one-dimensional electrode experiment was also used to determine E_{rp}, which corresponds to the average of E_{rp} of deep pits [49]. Once the experimental polarization scan and E_{rp} were determined, the integration of Equation (3.2) was performed with the experimentally-derived data.

The integrated experimental data and corresponding data fit are shown in Figure 3-2. The fit is found by minimizing the sum of squared errors after assuming a model that is logarithmic with respect to chloride concentration and linear with respect to temperature.

$$i_{eq} = -0.01.53 \ln Cl + 0.001458\, T, \tag{3.5}$$

Where the chloride concentration Cl has units of moles/liter, temperature T is in ℃, and i_{eq} has units A/m^2.

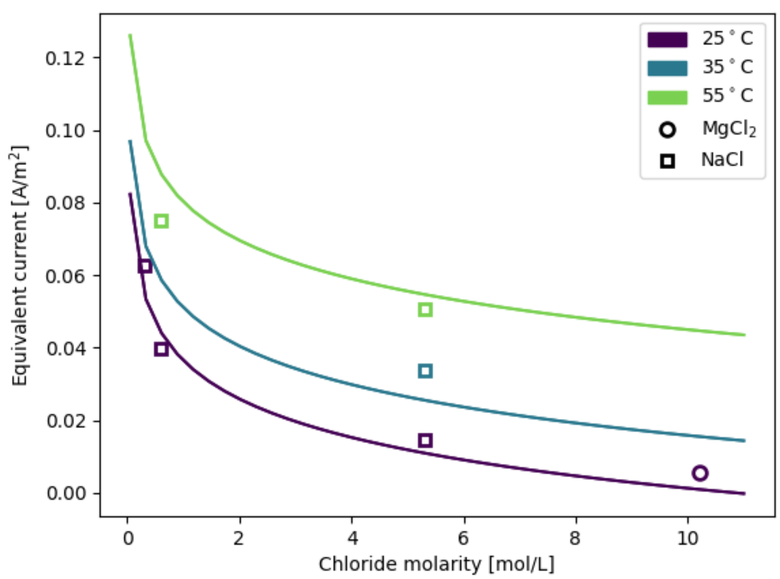

Figure 3-2. Experimental data and model fit for equivalent current density

The parametric model for I_{pit}/r_{pit} is replaced by a model that varies with local conditions. The model is parameterized using experimental data from [47, 46]. As previously mentioned, one-dimensional electrodes were utilized in order to determine $(i \cdot x)_{sf}$ with the method of Srinivasan and Kelly [49]. $(i \cdot x)_{sf}$ is then converted to I_a/r_a by a geometric factor of 3 [50].

The experimental data and corresponding data fit are shown in Figure 3-3. The fit is found by minimizing the sum of squared errors after assuming a model that is logarithmic with respect to chloride concentration and linear with respect to temperature.

$$\frac{I_{pit}}{r_{pit}} = 3PS(\,-0.3136 \ln Cl\, + 0.01068T + 0.562), \tag{3.6}$$

Where the pit stability product I_{pit}/r_{pit} is in A/m, temperature T is in °C, and chloride concentration Cl is in moles/liter. The term PS indicates percent saturation and accounts for the variation in necessary $FeCl_2$ saturation at the surface of the alloy within the pit for pit propagation. This value is expected to vary with bulk cation and temperature; a reasonable range of possible values is $0.4 \leq PS \leq 0.7$ [51, 52, 49], but it is set to 0.5 in this work. The first constant is a geometric parameter that is set to 3, which corresponds to conversion from one-dimensional to hemispherical pits. Though Equation (3.6) is based on data collected between $25°C \leq T \leq 55°C$, Jun et al. have shown that the linear trend in temperature is valid up to 85°C [53].

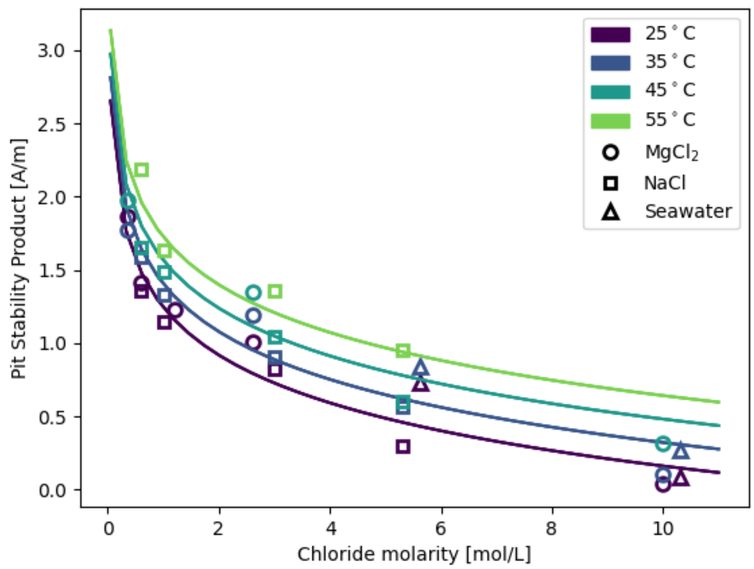

Figure 3-3. Experimental data and model fit for pit stability product

3.3 Implementation Comparison

The new experimentally-informed maximum pit size model will significantly impact the probabilistic SCC model because pit depth is a determining factor in crack initiation. Therefore, it is important to understand the integral effect that changes in i_{eq}, ΔE_{max}, and I_{pit}/r_{pit} will have on the maximum pit size. To document this effect, this section shows results for each of these parameters and the overall effect on pit size.

The equivalent anode current i_{eq}, potential drop ΔE_{max}, and pit stability criterion I_{pit}/r_{pit} are shown as a function of temperature and relative humidity in Figure 3-4, Figure 3-5, and Figure 3-6, respectively. The effect of these changes on the maximum pit size is shown in Figure 3-7. Each subfigure shows the maximum pit size for a different fixed value of deposition density. Overall, the new modeling approach results in larger maximum pit sizes by about an order of magnitude. This change should result in earlier crack initiation, since deeper pits correspond to larger tip stresses.

Finally, note that the new model is not probabilistic; the parameters in Equations (3.5) and (3.6) have not been assigned distributions. However, uncertainty could easily be incorporated into the new model by calibrating the model to the experimental data in Figure 3-2 and Figure 3-3.

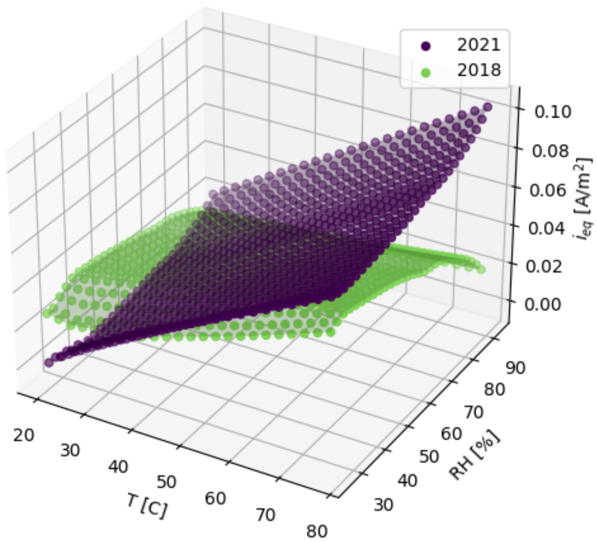

Figure 3-4. Anode equivalent current

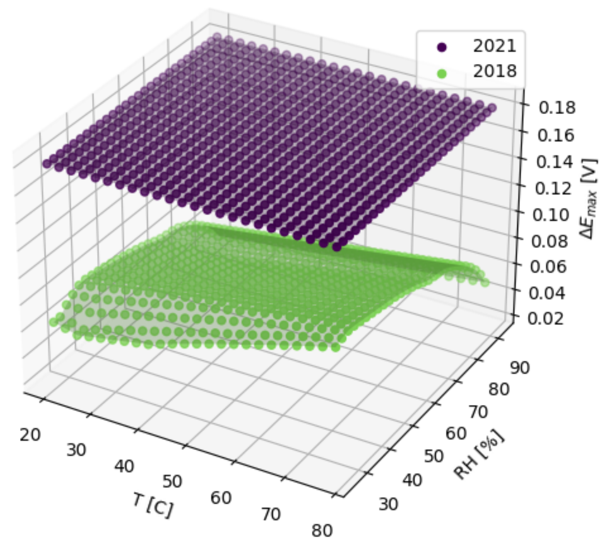

Figure 3-5. Potential drop

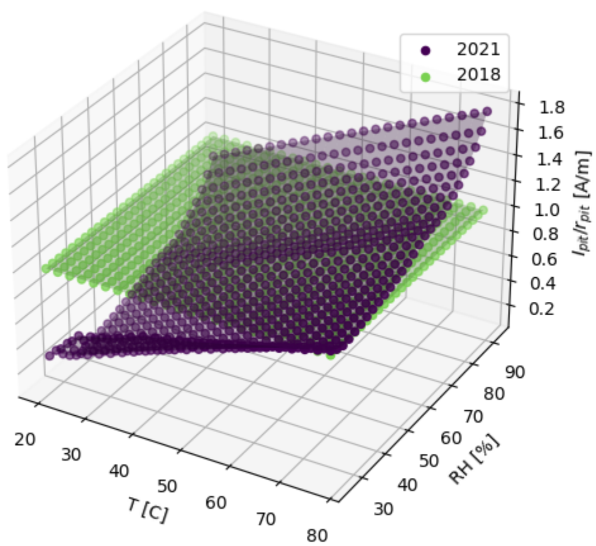

Figure 3-6. Pit stability criterion

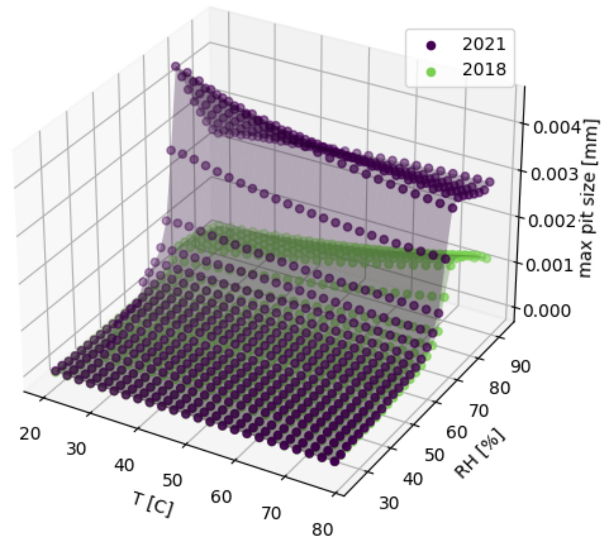

(a) 0.1 g/m²

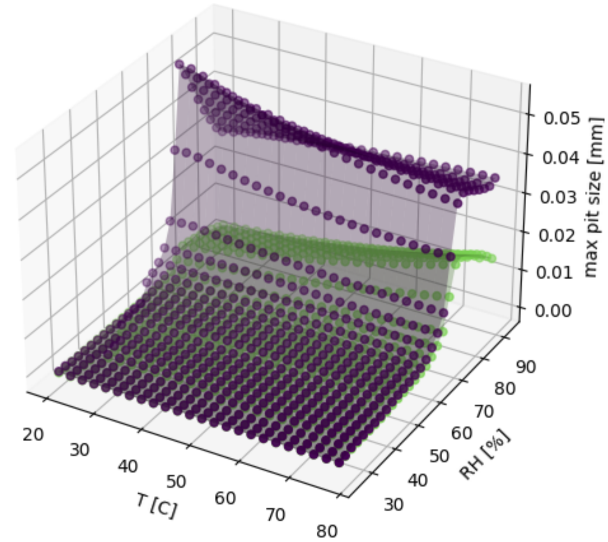

(b) 1 g/m²

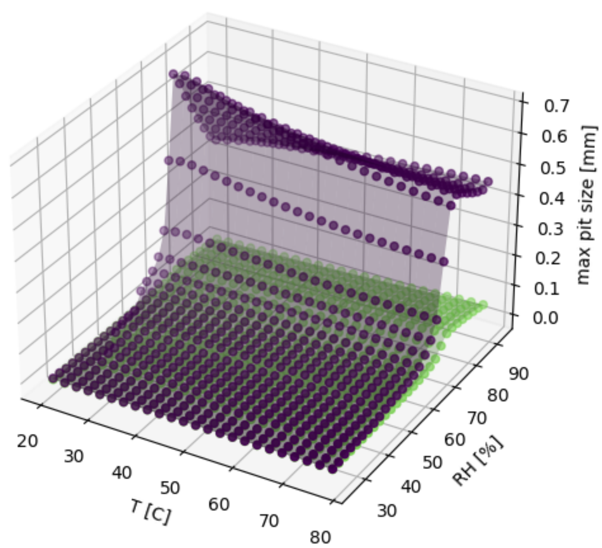

(c) 10 g/m²

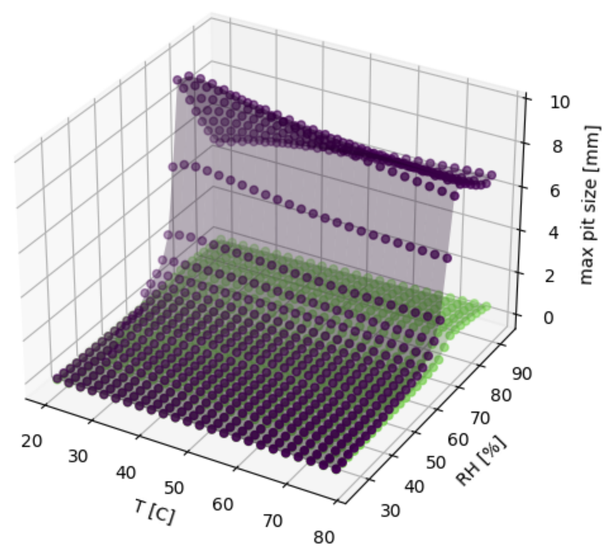

(d) 100 g/m²

Figure 3-7. Effect of model changes on calculated maximum pit size for different salt deposition

4. CRACK GROWTH RATE

The crack growth rate (CGR) model, as implemented in the SCC probabilistic model in 2018 [26], is defined by Equation (4.1).

$$\frac{dx_{crack}}{dt} = \dot{x} = \alpha \cdot exp\left[-\frac{Q}{R}\left(\frac{1}{T} - \frac{1}{T_{ref}}\right)\right] \cdot (K - K_{th})^{\beta} \tag{4.1}$$

where:

$\frac{dx_{crack}}{dt}$ is the crack growth rate (m/s), also denoted $\dot{x}$,

T is the temperature (K) of interest,
α is the crack growth amplitude,
β is the stress intensity factor exponent,
Q is the activation energy (J/mol) for crack growth,
R is the universal gas constant (8.314 J mol^{-1} K^{-1}),
T_{ref} is a reference temperature (K) at which α was derived ($15.55°\text{C} = 288.75\ K$ was used in this study),
K is the crack tip stress intensity factor, and
K_{th} is the threshold stress intensity factor for SCC.

Realistically, crack growth depends on additional factors which are not explicitly included in this model, such as the degree of sensitization, yield stress, chloride concentration, the mass of chloride per unit surface area, and solution pH. However, the experimental data used to calibrate the model contain variation in all of these factors, so the factors still contribute to uncertainty in the model [23].

The calibration of the 2018 model was based on CGR data for atmospheric corrosion at a narrow range of temperatures [28]. In this report, additional atmospheric data and new immersed data are incorporated into the calibration process. The CGR model calibration to experimental data is described in Section 4.1 and a description and test of the code implementation is given in Section 4.2.

4.1 Calibration

The CGR model is implemented within the SCC probabilistic model to include uncertainty in α and β via uncertainty distributions, which are determined by a combination of assumptions and calibration to the immersed and atmospheric experimental data. The $K - K_{th}$ term was set equal to 50 for this calibration, as in previous iterations [23]. Hence, T is the independent variable; α, β, and Q are parameters; and R, T_{ref}, K, and K_{th} are constants.

The SCC probabilistic model is a function of temperature and the calibration depends on data at multiple temperatures. The CGR model is calibrated using experimentally measured rates, which are categorized under two conditions: atmospheric, immersed.

- Atmospheric data come from studies in which salt is deposited on a metal surface and exposed to a humid atmosphere. Salt deposition was either observed from natural exposure [54, 55] or induced by application of mist [54, 56, 57], droplets [58, 59, 60, 61], or submersion [62] followed by evaporation. The applied salts were sea salts [54, 59, 61, 63, 64], magnesium chloride ($MgCl_2$) [56, 59, 60, 62, 63, 65], or sodium chloride (NaCl) [54, 58] in varying concentrations. In addition to the artificial atmospheric corrosion data, some operational data exists for crack growth rates on DSCs [66].
- Immersed data come from studies in which the specimens were kept immersed in a solution intended to mimic marine environments. This includes $MgCl_2$ solutions [55, 67], NaCl solutions [67], substitute ocean water [68], sea salts [69], and mixtures of NaCl, sodium sulfate (Na_2SO_4), and hydrogen chloride (HCl) [70].

All of the atmospheric and immersed data described above are for 304 stainless steel. Data also exist for 316 stainless steel, and though these data were not included in the calibration they are included in Figure 4-1 for comparison [71, 72, 73, 74, 75].

All data are plotted in Figure 4-1 as the natural logarithm of the experimentally measured crack growth rate versus the reciprocal of the temperature. The atmospheric and immersed data follow similar trends, which appear clearly linear in this space. This linear relationship forms the basis for the CGR model and its calibration. Though the two categories of data follow a similar pattern, the immersed data are measured using more accurate techniques, and are therefore considered more representative, so calibration is performed to preferentially weight or emphasize the immersed data compared to the atmospheric data.

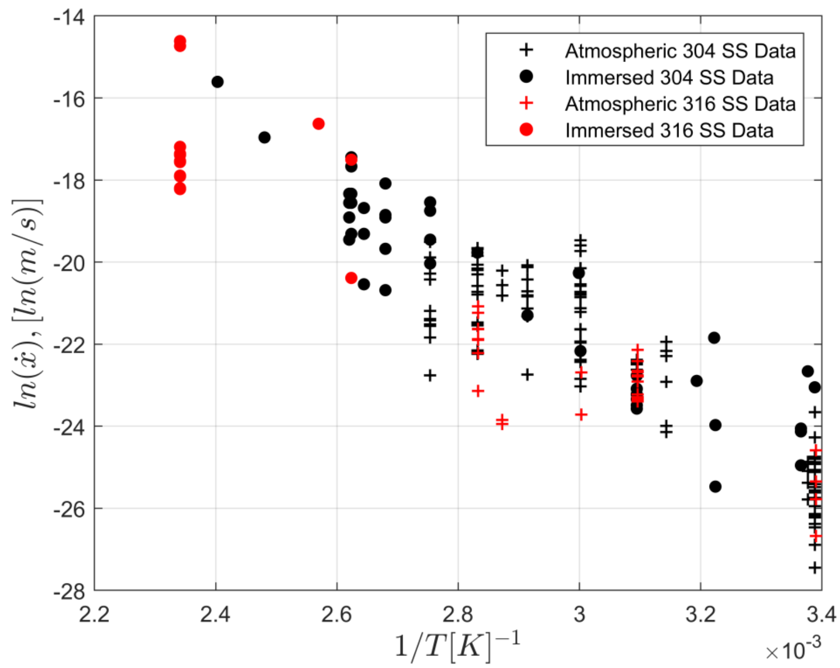

Figure 4-1 The experimental data used to calibrate the CGR model demonstrate a distinctive linear trend when plotted as the natural logarithm of the crack growth rates versus the reciprocal temperature.

The experimental and operational data used to calibrate the CGR model contain averages with high/low values or standard deviations. For this iteration of the calibration, the average, high, and low values are all treated as individual data points. Standard deviations were not used due to lack of information about the underlying distribution; a mean and standard deviation are only adequately descriptive if describing a normal or lognormal distribution. The consequence of this treatment of the data is that the standard deviation of the final model will be wider even though there is a relatively large number of data points. Essentially, the data confer information both about the trend the model should follow, but also how much uncertainty should be included in it. Future development of the calibration method for this model should investigate other options for this data; one option could be to use only the means to fit the general trend, but determine the standard deviation of the final model using the min/max and standard deviation values, perhaps assuming that the min/max values represent two standard deviations.

Two methods were tested for calibrating the CGR, one using a standard linear regression analogous to previous calibrations and one using Bayesian statistics. Both methods are presented here with a discussion comparing them, though more attention is given to the method based on linear regression since it is the least subjective of the two.

4.1.1 Linear Regression Calibration

Conceptually, the linear regression calibration seeks to identify the best linear model for the data in Figure 4-1, with uncertainty, and uses this model to propagate parameter estimates through (4.1) using a sequence of assumptions. The basic process is to define normal distributions at two temperatures. These distributions can then be sampled with β to estimate α and Q. The initial process of defining the normal distributions was completed using the following steps:

1. Fit a standard least squares linear regression to the immersed data plotted in Figure 4-1. For a temperature T_i, this model has the form:
$$\hat{y}(T_i) = m_{Immersed}\frac{1}{T_i} + b_{Immersed} \tag{4.2}$$
where $m_{Immersed}$ and $b_{Immersed}$ are determined using least squares, and $\hat{y}_i$ denotes the model estimate for $\ln{(\dot{x})}$ at $T = T_i$.
2. Calculate the residual, $r_i = \ln{(\dot{x}_i)} - \hat{y}_i$, for every $\dot{x}_i$ in the data set (atmospheric and immersed). The residuals characterize how far the predictions of the linear regression are from the true values in the data.
3. Fit a second standard linear regression, this time between the predictions and the absolute values of the residuals, $|r_i|$, and evaluate $\hat{y}_i$ at each prediction to estimate the standard deviation. This model can be expressed as:
$$\hat{\sigma}_i = m_\sigma \hat{y}_i + b_\sigma \tag{4.3}$$
where m_σ and b_σ are again determined using least squares. This step characterizes a systematic relationship between the predictions and the residuals as a model for the standard deviation of data at each temperature. If there were many repeated measurements at each temperature, this step would be unnecessary since standard deviation would be calculated directly in that case.
4. Use the estimates of standard deviation, $\hat{\sigma}_i$, to define a weight for every data point as:
$$w_i = \frac{1}{\sigma_i} \tag{4.4}$$
This method for defining weights assigns the highest weight to data that are close to Equation (4.2), which is the linear model that was fit to only immersed data.
5. Fit a final linear regression predicting crack growth rate as a function of the reciprocal temperature using weighted least squares. In essence, this step re-fits the model in Equation (4.2) using non-equal weights for the data points. This regression was performed in MATLAB 2020a using the `lscov` function [76, 77]. As in (4.2), this model has the form:
$$\hat{y}(T) = m_{Final}\frac{1}{T} + b_{Final} \tag{4.5}$$
where m_{Final} and b_{Final} are determined using weighted least squares. Note that this method also provides the mean squared error, MSE, which is used to estimate the standard deviation of the final model.
6. Let $T_1 = 15.55°\text{C} = 288.71K$ and $T_2 = 80°\text{C} = 353.15K$. Define the following distributions at these two temperature test points using the results of the final linear regression:
$$\ln{[\dot{x}(T_1)]} \sim Normal\left(m_{Final}\frac{1}{T_1} + b_{Final}, \sqrt{MSE}\right) \tag{4.6}$$
$$\ln{[\dot{x}(T_2)]} \sim Normal\left(m_{Final}\frac{1}{T_2} + b_{Final}, \sqrt{MSE}\right) \tag{4.7}$$

These first six steps effectively establish the model. All that remains is to sample from the distributions in (4.6) and (4.7), and then apply (4.1) with some assumptions to convert these crack growth rate samples into samples for the model parameters. The sampling procedure described in the following steps results in a final distribution on α, which is input to the SCC probabilistic code. Steps are also included to produce the resulting sample distributions for the crack growth rate and Q for evaluation of the calibration quality before applying to the SCC probabilistic model. The calibration sampling steps are:

1. Denote samples from Equation (4.6) as ln ($\dot{x}_{15C}$) and denote samples from Equation (4.7) as ln ($\dot{x}_{80°C}$). Sample values for ln ($\dot{x}_{15°C}$) and ln ($\dot{x}_{80°C}$) from (4.6) and (4.7) respectively and calculate the line between these two points. This line defines the model for that sample realization:

$$\ln\,[\dot{x}(\mathrm{T})] = m_{sample}\frac{1}{T} + b_{sample} \tag{4.8}$$

2. Also sample a value, β_{sample}, for β from (4.2). As in previous iteration of the CGR model [23], β is sampled from a normal distribution, $\beta \sim N(\mu = 0.5, \sigma = 0.2)$ truncated to $[0, 1]$.
3. Assume that $T = T_{Ref} = 15.55$°C and use this assumption with (4.1) to obtain the value of α_{sample}. Expressing (4.1) in terms of samples, this calculation is:

$$\dot{x}_{15C} = \alpha_{sample} \cdot (K - K_{th})^{\beta_{sample}} = \alpha_{sample} \cdot 50^{\beta_{\mathrm{sample}}} \tag{4.9}$$

$$\alpha_{sample} = \frac{\dot{x}_{15C}}{50^{\beta_{sample}}} \tag{4.10}$$

4. Use the samples α_{sample}, β_{sample}, and $\dot{x}_{80°C}$ to calculate the resulting sample for activation energy:

$$Q_{sample} = \frac{-R}{\frac{1}{353.25} - \frac{1}{T_{Ref}}} \ln\left(\frac{\dot{x}_{80C}}{\alpha_{sample} \cdot 50^{\beta_{sample}}}\right) \tag{4.11}$$

5. Apply (4.1) to α_{sample}, β_{sample}, and Q_{sample} to calculate the final sample for the crack growth rate for this sample realization at any temperature, T:

$$\frac{dx_{crack}}{dt} = \dot{x} = \alpha_{sample} \cdot exp\left[-\frac{Q_{sample}}{8.314}\left(\frac{1}{T} - \frac{1}{288.71}\right)\right] \cdot (50)^{\beta_{sample}} \tag{4.12}$$

The result of this calibration is shown in Figure 4-2. The plot includes 95% bounds on the model and each of the grey lines represents one realization of the model; 100 out of 100,000 total realizations are plotted. Rank correlation was applied between α and β to plot the calibration results since correlation is applied within the SCC probabilistic model. This is why the variation in the slopes of the model realizations in the plot is lower than would otherwise be expected due to $\dot{x}_{15°C}$ and $\dot{x}_{80°C}$ being sampled independently. This is an analysis step meant to support the calibration; the actual results from the implemented CGR model with these parameters are presented in Section 4.2.

The distribution on Q is not a calibration; it results from the sampled values for α and β and the correlation imposed between the parameters. The Q distribution is reported to support analysis of reasonableness of the model. The mean value for Q that results from the model seems reasonable when compared to activation energies reported in the literature for sensitized Type 304 stainless steel (e.g. 50-65 kJ/mol [78] and 58.8 kJ/mol [79]). Overall, the new calibration results in slightly more uncertainty in the CGR, which is representative of the additional data.

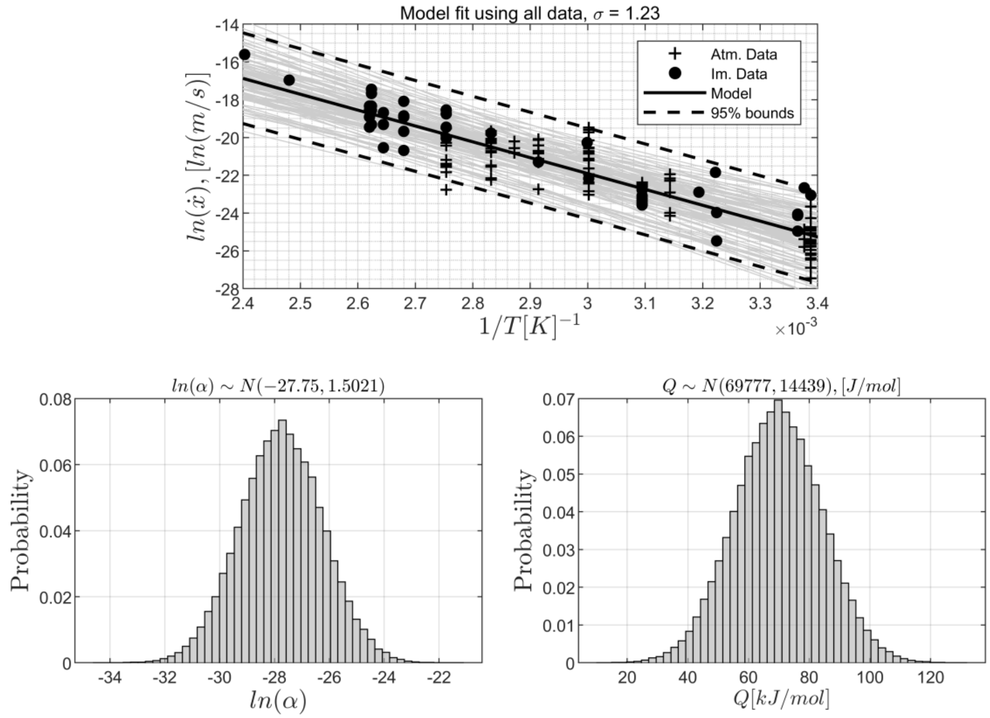

Figure 4-2 The final model from the linear regression method trends consistently with the data. These results are plotted including a rank correlation between α and β, which somewhat limits variability in the slope of the linear model. Q is not calibrated, but its distribution results from the uncertainty in α and β and the imposed correlation between them.

4.1.2 Bayesian Calibration

The calibration method discussed in Section 4.1.1 calibrates the uncertainty distribution for α based on evaluation of the model at $T = T_{ref}$, and the procedure for performing the calibration is complex since it requires a sequence of modeling steps, assumptions, and evaluations at particular points. One option for simplifying the calibration is to simultaneously calibrate all of the parameters. Implementation of the same model in Bayesian software treats α, β, Q, and the standard deviation of the final model as hyperparameters that are simultaneously calibrated using Gibbs sampling [80].

This calibration was implemented using the JAGS software [81]. The log of (4.1) was defined as the mean of a normal distribution with standard deviation σ, analogous to the final model from Section 4.1.1. In a Bayesian calibration, the parameters (α, β, Q, and σ) are all assigned prior assumed distributions meant to reflect the current state of knowledge about those parameters. The sampling procedure then compares the model form to the data to refine/shift/stretch/reshape those distributions as dictated by the data.

This type of calibration necessarily includes some subjectivity in the model results. If the prior distributions are highly specific, the data may not have as much power over the final model as it should. If the prior distributions are too broad, the data may not be sufficient to result in a meaningful final model. Ideally, there should either be some reasonable justification for prior values, or it should be demonstrated that the final model is not highly sensitive to the subjective prior selection.

The ability to include expert judgement or prior knowledge in a Bayesian calibration using prior distributions is valuable in some cases, but for the CGR model, the goal is to rely on the plentiful data and not subjective judgements. Thus, the Bayesian calibration was attempted with broad (i.e. uninformed) prior distributions but failed to converge to a useful result. The distributions were refined, essentially by using the methods in Section 4.1.1 to estimate them, but then the Bayesian calibration did not change the prior distributions at all, making this method of calibration essentially equivalent to Section 4.1.1.

Bayesian calibration may still have some utility for this model in the future, especially if more relevant data are published, but it did not confer any benefit over the method in Section 4.1.1 in this analysis.

4.2 Implementation

To implement the calibrated model in Section 4.1.1, three uncertain distributions are sampled at each epistemic code loop: α, β, and $\dot{x}_{80°C}$. This approach is the same as the 2018 model, but with slightly different definitions for the three parameters. A comparison between the 2018 and 2021 parameter distributions is shown in Table 2.

Table 2. Comparison of CGR parameterization between 2018 and 2021 models. Note that, to avoid sampling in the distribution tails, all distributions are truncated at two standard deviations.

Parameter	2018 Model	2021 Model
$\ln \alpha$	$N(-25.92, 1.57)$	$N(-27.75, 1.50)$
β	$N(0.5, 0.2)$	$N(0.5, 0.2)$
α-β correlation	-0.47	-0.50
$\dot{x}_{80°C}$	$N(-20.14, 1.33)$	$N(-20.50, 1.23)$

Similar to the 2018 approach, α and β are correlated after being sampled. This process starts with two random samples from the standard normal distribution $N(0,1)$, which will be called X_1 and X_2[b]. According to [82], these standard normal samples can be transformed to correlated normal variables with a desired mean and standard deviation (in this case, α and β) by defining a third random variable X_3.

$$X_3 = \rho X_1 + \sqrt{1-\rho^2} X_2, \tag{4.13}$$

Where the desired correlation is ρ. Then, samples from the correlated distributions of α and β can be calculated.

$$\beta_{sample} = \mu_\beta + \sigma_\beta X_3 \tag{4.14}$$

$$\alpha_{sample} = \mu_\alpha + \sigma_\alpha X_1, \tag{4.15}$$

Where μ_β and σ_β are the desired mean and standard deviation of β. Similarly, μ_α and σ_α are the desired mean and standard deviation of α.

A comparison between the 2018 and 2021 implementations is shown in Figure 4-3[c]. The top row shows the two models as a function of inverse temperature. For comparison, the experimental data for each calibration is also included in the plots. For each model, 5,000 samples are taken from the model at random temperatures and are colored by point density, which allows easy visualization of the sampled data. Finally, the sampled linear trends are also shown, which allows comparison with Figure 4-2. As

[b] Note that the 2018 implementation incorrectly sampled these distributions from $N(\mu_\alpha,\sigma_\alpha)$ and $N(\mu_\beta, \sigma_\beta)$, which resulted in the wrong crack growth rates. This error has been corrected by transforming the samples to standard normal, then correctly applying the correlation methodology. The code results shown in Figure 4-3 for the 2018 model were generated after implementing the code fix.

[c] The samples shown in Figure 4-3 are actual output from the Fortran source code. This serves as a test of the model implementation, as the samples are representative of the experimental data.

noted in Section 4.1, the new correlation parameterization results in more uncertainty in the CGR. The wider uncertainty range is representative of the new data, which has more variability than the old data.

The second row of plots in Figure 4-3 shows the relationship between α and β. Though there is a clear correlation between the two variables, it is not as drastic as the correlation used in Equation (4.13). The target value for the old model is -0.47 and the new model is -0.50, whereas the actual correlations are both about -0.2. This discrepancy is primarily caused by the application of the correlation process to truncated normal distributions instead of standard normal distributions. In addition, the process described in Equations (4.13)-(4.15) is approximate with some error. Though the samples seem correlated enough to correctly match the experimental data, this lack of correlation may have an impact on the behavior of CGR as the stress intensity factor K varies. Therefore, properly implementing the correlation remains a topic for future study.

The final row of plots in Figure 4-3 shows the probability density function of Q for the 2018 and 2021 models. This plot is included to show that the updated distribution for sampling $\dot{x}_{80°\mathrm{C}}$ results in a distribution for Q that is similar to the old model. The new distribution of Q is slightly narrower and is centered higher than the previous distribution. Most notably, this avoids the negative values of Q that were permitted in the old model. Note that the $\dot{x}_{80°\mathrm{C}}$-α or $\dot{x}_{80°\mathrm{C}}$-β correlations are not accounted for in the sampling scheme. This lack of correlation causes a wider distribution for Q than in the calibration (see Figure 4-2). Since Q has more variance, a wider range of slopes are seen in the model. However, the sampling scheme still matches relatively well with the underlying data. Improving the sampling scheme remains a topic for future study.

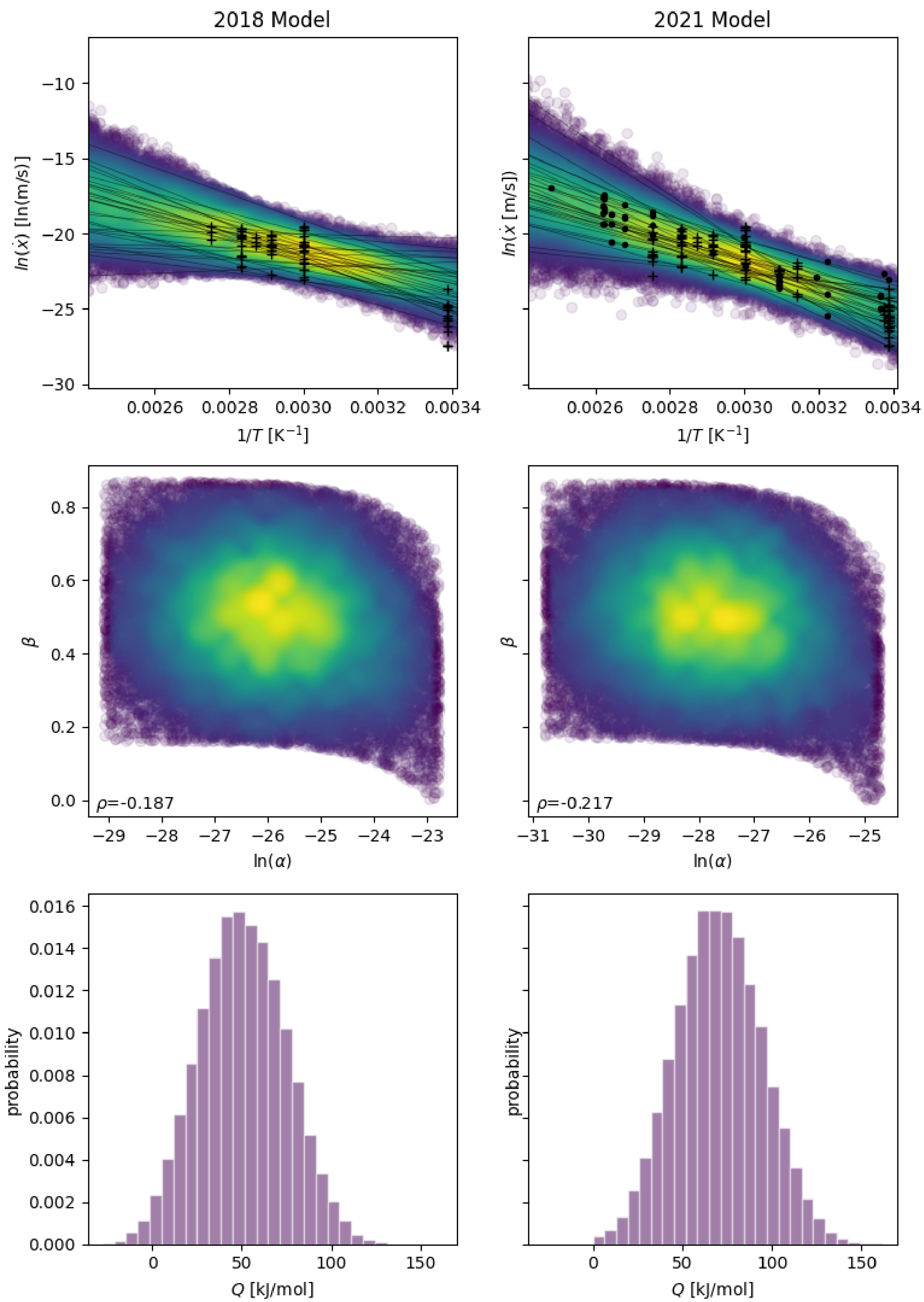

Figure 4-3. Sample results of new CGR model implementation

5. Conclusion and Future Work

In this report, three major model updates were described for probabilistic modeling of SCC of DSCs: salt deposition model, maximum pit size, and CGR calibration. All three updates constitute major changes to the modeling approach and will have an impact on predicted SCC quantities of interest; however, the overall effect remains a topic for future study. Currently, the changes to the salt deposition and maximum pit size models have opposing effects on maximum pit size predictions. Since changes to the maximum pit size will impact the timing of crack initiation, these model changes may have drastic effects on the overall model predictions. Though the crack growth rate model has been re-calibrated and the model has more experimental justification, the new parameter distributions are not expected to have a significant impact on the code predictions.

If additional experimental data become available, significant work remains to properly implement an accurate salt deposition model with uncertainty. Critical data will be collected by the Canister Deposition Field Demonstration project, a 10-year project to evaluate dust deposition onto dry storage canisters. However, these data will not begin to be available for 3-4 years, at the earliest. Therefore, efforts in the near future will focus on incorporating the functional relationship between salt deposition rates and ocean proximity. An approach that incorporates available site-specific data relating to proximity to the ocean and canister orientation could be possible. Because the available data are sparse, experimental results for other surfaces may be useful to inform an appropriate uncertainty range on the parameterization.

The maximum pit size model has been completely reformulated and now predicts much larger pits. An obvious next step would be to incorporate uncertainty by calibrating the new model to experimental data. The new model is specific to 304L stainless steel, the most common SNF dry storage canister material. The model calibration could incorporate more experimental data, which would expand the range of applicability and better inform the uncertainty of the model.

Future work for the crack growth rate model may include gathering additional data and more advanced statistical treatment of the data. The current study treats minimums, maximums, and means as equivalent data points. This treatment of the data inflates uncertainty around the crack growth rate trend with respect to the reciprocal temperature. Alternative formulations of these data require assumptions since these statistics are often reported without sufficient information of the underlying distribution. Future work could examine the most justifiable assumptions on the data and re-calibrate the model under those assumptions. Additionally, current calibration of the crack growth rate model occurs in distinct stages where the values of some parameters are estimated as specific points on the model (e.g. α when $T = T_{ref}$) . This creates a circular process within the model calibration; it may be more efficient and clearer to apply a different approach to calibration that can simultaneously calibrate all parameters.

The model updates that are presented here have not yet been propagated through the entire probabilistic SCC model. Each of these changes could have a large effect on the model predictions. The changes to the maximum pit size model yield significantly different maximum pit sizes than the previous model, which will impact the necessary salt load for pit-to-crack transition. The changes to the crack growth rate model only have a small impact on predicted crack growth rates compared to the previous model. However, an error in the previous model implementation, discovered while implementing the new model, means that the new CGR model may have a significant effect on code outputs of canister penetration. Finally, the predictions of dust deposition onto the canisters in the previous iteration of the probabilistic SCC model were recognized to be orders of magnitude higher than the available data. Because the model predictions and the observational data could not be reconciled, it was decided to parameterize the dust deposition rate.

6. References

[1] NRC, "Storage of Spent Nuclear Fuel," 3 May 2021. [Online]. Available: https://www.nrc.gov/waste/spent-fuel-storage.html. [Accessed 6 July 2021].

[2] NRC, *10 CFR Part 71-Packaging and Transportation of Radioactive Material,* Washington DC, March 2021. www.nrc.gov/reading-rm/doc-collections/cfr/part071/.

[3] NRC, *10 CFR Part 72-Licensing Requirements for the Independent Storage of Spent Nuclear Fuel, High-Level Radioactive Waster, and Reactor-Related Greater than Class C Waste,* Washington DC, September 2020. www.nrc.gov/reading-rm/doc-collections/cfr/part072/.

[4] NRC, *Regulatory Guide 3.50-Standard Format and Content for a Specific License Application for an Independent Spent Fuel Storage Installation or Monitored Retrievable Storage Facility,* Washington DC, 2014. www.nrc.gov/docs/ML1404/ML14043A080.pdf.

[5] NRC, *Regulatory Guide 3.62-Standard Review Plan for Spent Fuel Dry Storage Systems at a General License Facility,* Washington DC, 2014. www.nrc.gov/docs/ML0037/ML003739545.pdf.

[6] NRC, "Standard Review Plan for Spent Fuel Dry Storage Systems at a General License Facility," NUREG-1536, Washington DC, 2010. www.nrc.gov/docs/ML1010/ML101040620.pdf.

[7] NRC, "Standard Review Plan for Spent Fuel Dry Storage Facilities," NUREG-1567, Washington DC, 2020. www.nrc.gov/docs/ML0036/ML003686776.pdf.

[8] J. J. Lichtenwalter, S. M. Bowman, M. D. DeHart and C. M. Hopper, "Criticality Benchmark Guide for Light Water Reactor Fuel in Transportation and Storage Packages," NUREG/CR-6361 ORNL/TM-13211, SNL, Washington DC, 1997. www.nrc.gov/docs/ML0108/ML010820352.pdf.

[9] S. M. Bowman, I. C. Gauld and J. C. Wagner, "Recommendations on Fuel Parameters for Standard Technical Specifications for Spent Fuel Storage Casks," NUREG/CR-6716 ORNL/TM-2000/385, NRC and ORNL, Washington DC, March 2001. www.nrg.gov/docs/ML0108/ML010820352.pdf.

[10] NRC Division of Spent Fuel Storage and Transportation, *Interim Staff Guidance 1: Classifying the Condition of Spent Nuclear Fuel for Interim Storage and Transportation Based on Function,* Washington DC, May 2007. www.nrc.gov/docs/ML0714/ML071420268.pdf.

[11] NRC Spent Fuel Project Office, *Interim Staff Guidance 11: Cladding Considerations for the Transportation and Storage of Spent Fuel,* Washington DC, November 2003. www.nrc.gov/reading-rm/doc-collections/isg/isg-11R3.pdf.

[12] NRC Division of Spent Fuel Management, *Interim Staff Guidance 2: Fuel Retrievability in Spent Fuel Storage Applications,* Washington DC, April 2016. www.nrc.gov/docs/ML0714/ML071420268.pdf.

[13] J. Bruno and R. C. Ewing, "Spent Nuclear Fuel," *Elements,* vol. 2, no. 6, pp. 343-349, December 2006. doi: 10.2113/gselements.2.6.343.

[14] Kain, "Marine Atmospheric Stress Corrosion Cracking of Austenitic Stainless Steels," *Materials Performance,* vol. 29, no. 12, pp. 60-62, December 1990.

[15] K. Shirai, J. Tani, T. Arai, M. Wataru, H. Takeda and T. Saegusa, "SCC Evaluation Test of a Multi-Purpose Canister," in *Proceedings of the 13th International High-Level Radioactive Waste Management Conference (IHLRWMC)*, LaGrange Park IL, April 10-14, 2011.

[16] NRC, "Finite Element Analysis of Weld Residual Stresses in Austenitic Stainless Steel Dry Cask Storage System Canisters," NRC Technical Letter Report (ADAMS ML13330A512). Nuclear Regulatory Commission, 2013.

[17] D. Enos and C. Bryan, "Final Report: Characterization of Canister Mockup Weld Residual Stresses," FCRD-UFD-2016-000064, U.S. DOE, 2016.

[18] EPRI, "Calvert Cliffs Stainless Steel Dry Storage Canister Inspection," p. 460, 2014.

[19] C. Bryan and D. Enos, "Analysis of Dust Samples Collected from Spent Nuclear Fuel Interim Storage Containers at Hope Creek, Delaware, and Diablo Canyon, California," SAND2014-16383, Sandia National Laboratories, p. 281, 2014.

[20] C. Bryan and D. Enos, "Analysis of Dust Samples Collected from an In-Service Interim Storage System at the Maine Yankee Nuclear Site," SAND2016-10266, Sandia National Laboratories, p. 51, 2016.

[21] C. Bryan and E. Schindelholz, "Analysis of Samples Collected from the Surface of Interim Storage Canisters at Calvert Cliffs in June, 2017: Revision 01," SAND2017-12429, Sandia National Laboratories, p. 26, 2017.

[22] M. Teague, S. Saltzstein, B. Hanson, K. Sorenson and G. Freeze, "Gap Analysis to Guide DOE R&D in Supporting Extended Storage and Trasnportation of Spent Nuclear Fuel: An FY2019 Assessment," SAND2019:15479, US Department of Energy, Washington DC, 2019.

[23] R. Dingreville, C. J. Sallaberry, C. R. Bryan, C. Stockman, H. Adkins and M. Sutton, "Uncertainty Quantification Methodologies Development for Storage and Transportation of Used Nuclear Fuel: Pilot Study on Stress Corrosion Cracking of Canister Welds," OUO/ECI SAND2014-19467, SNL, Albuquerque NM, 2014.

[24] C. R. Bryan, C. J. Sallaberry, R. Dingreville, C. T. Stockman, H. Adkins and M. Sutton, "Probabilistic Performance Assessment: SCC of SNF Interim Storage Canisters," in *Proceedings of the International High-Level Radioactive Waste Management (IHLRWM) Conference*, Charleston SC, April 2015.

[25] R. Dingreville and C. R. Bryan, "Uncertainty Quantification Methodologies Development for Stress Corrosion Crack of Canister Welds," SAND2016-9487R, SNL, Albuquerque NM, 2016.

[26] C. J. O'Brien, C. Alexander, C. R. Bryan, E. J. Schindelholz and R. Dingreville, "Status Report: Uncertainty Quantification of Environmentally Assisted Stress Corrosion Cracking in Used Fuel Canisters," SAND2019-3600R, SNL, Albuquerque NM, 2019.

[27] D. G. Enos, C. R. Bryan and K. M. Norman, "Data Report on Corrosion Testing of Stainless Steel SNF Storage Canisters," SAND2013-8314P, SNL, Albuquerque NM, 2013.

[28] C. R. Bryan and D. Enos, "Summary of Available Data for Estimating Chloride-Induced SCC Crack Growth Rates for 304/316 Stainless Steel," SAND2016-2992R, SNL, Albuquerque NM, March 2016.

[29] J. Alcantara, B. Chico, I. Diaz, D. de la Fuente and M. Morcillo, "Airborne Chloride Deposit and Its Effect on Marine Atmospheric Corrosion of Mild Steel," *Corrosion Science,* vol. 97, pp. 74-88, August 2015. doi: 10.1016/j.corsci.2015.04.015.

[30] S. Li and L. H. Hihara, "Aerosol Salt Particle Deposition on Metals Exposed to marine Environments: A Study Related to Marine Atmospheric Corrosion," *Journal of the Electrochemical Society,* vol. 161, no. 5, pp. C268-C275, April 2014. doi: 10.1149/2.071405jes.

[31] I. O. Wallinder, X. Zhang, S. Goidanich, N. le Bozec, G. Herting and C. Leygraf, "Corrosion and Runoff Rates of Cu and Three Cu-Alloys in Marine Environments with Increasing Chloride Deposition Rate," *Science of the Total Environment,* vol. 472, pp. 681-694, February 2014. doi: 10.1016/j.scitotenv.2013.11.080.

[32] E. Schindelholz, R. G. Kelly, I. S. Cole, W. D. Ganther and T. H. Muster, "Comparability and Accuracy of Time of Wetness Sensing Methods Relevant for Atmospheric Corrosion," *Corrosion Science,* vol. 67, pp. 233-241, February 2013. doi: 10.1016/j.corsci.2012.10.026.

[33] F. Corvo, T. Perez, L. R. Dzib, Y. Martin, A. Castaneda, E. Gonzalez and J. Perez, "Outdoor-Indoor Corrosion of Metals in Tropical Coastal Atmospheres," *Corrosion Science,* vol. 50, no. 1, pp. 220-230, January 2008. doi: 10.1016/j.corsci.2007.06.011.

[34] I. S. Cole, D. Lau and D. A. Paterson, "Holistic Model for Atmospheric Corrosion Part 6: From Wet Aerosol to Salt Deposit," *Corrosion Engineering, Science, and Technology,* vol. 39, no. 3, pp. 209-218, November 2004. doi: 10.1179/147842204X2880.

[35] I. S. Cole and D. A. Paterson, "Holistic Model for Atmospheric Corrosion Part 5 - Factors Controlling Deposition of Salt Aerosol on Candles, Plates, and Buildings," *Corrosion Engineering, Science, and Technology,* vol. 39, no. 2, pp. 125-130, June 2004. doi: 10.1179/147842204225016949.

[36] M. A. Mustafa and K. M. Yusof, "Atmospheric Chloride Penetration into Concrete in Semitropical Marine Environment," *Cement and Concrete Research,* vol. 24, no. 4, pp. 661-670, 1994. doi: 10.1016/0008-8846(94)90190-2.

[37] V. N. Piskunov, "Parameterization of Aerosol Dry Deposition Velocities onto Smooth and Rough Surfaces," *Journal of Aerosol Science,* vol. 40, no. 8, pp. 664-679, 2009. doi: 10.1016/j.jaerosci.2009.04.006.

[38] EPRI (Electric Power Research Institute), "Susceptibility Assessment Criteria for Chloride-Induced Stress Corrosion Cracking (CISCC) of Welded Stainless Steel Canisters for Dry Cask Storage Systems," EPRI. EPRI-3002005371, Palo Alto CA, Sep 2015.

[39] P. Jensen, S. Suffield and B. Jensen, "Status Update: Deposition Modeling for SNF Canister CISCC," PNNL-30793, PNNL, Richland WA, December 2020.

[40] M. Mayuzumi, J. Tani and T. Arai, "Chloride Induced Stress Corrosion Cracking of Candidate Canister Materials for Dry Storage of Spent Nuclear Fuel," *Nuclear Engineering and Design,* vol. 238, no. 5, pp. 1227-1232, May 2008. doi: 10.1016/j.nucengdes.2007.03.038.

[41] Z. Y. Chen, F. Cui and R. G. Kelly, "Calculations of Cathodic Current Delivery Capacity and Stability of Crevice Corrosion Under Atmospheric Environments," *Journal of the Electrochemical Society,* vol. 155, no. 7, pp. C360-C368., May 2008. doi:10.1149/1.2926557.

[42] Z. Y. Chen and R. G. Kelly, "Computational Modeling of Bounding Conditions for Pit Size on Stainless Steel in Atmospheric Environments," *Journal of the Electrochemical Society,* vol. 157, no. 2, p. C69, 2010. doi:10.1149/1.3261803.

[43] C. R. Bryan, E. J. Schindelholz and C. Alexander, "Physical and chemical properties of sea-salt25 deliquescent brines as a function of relative humidity," 2018. Submitted.

[44] A. Anderko, N. Sridhar and D. S. Dunn, "A General Model for the Repassivation Potential as a Function of Multiple Aqueous Solution Species," *Corrosion Science,* vol. 46, no. 7, pp. 1583-1612, July 2004. doi: 10.1016/j.corsci.2003.10.002.

[45] C. L. Alexander and E. J. Schindelholz, "Cathodic Kinetics on Stainless Steel in Concentrated NaCl," 2018. In preparation.

[46] R. M. Katona, A. W. Knight, E. J. Schindelholz, C. R. Bryan, R. F. Schaller and R. G. Kelly, "Quantitative Assessment of Environmental Phenomena on Maximum Pit Size Predictions in Marine Environments," *Electrochimica Acta,* vol. 370, p. 137696, December 2020. doi:10.1016/j.electacta.2020.137696.

[47] R. M. Katona, J. Carpenter, E. J. Schindelholz and R. G. Kelly, "Prediction of Maximum Pit Sizes in Elevated Chloride Concentrations and Temperatures," *Journal of the Electrochemical Society,* vol. 166, no. 11, p. C3364, 2019. doi:10.1149/2.0451911jes.

[48] C. Liu and R. G. Kelly, "Comparison Study of the Effect of Oxide Film Properties on Cathodic Kinetics of Stainless Steel 304L and 316L During ORR Potential Window in Sulfate Solution," *Corrosion,* vol. 75, pp. 1087-1099, 2019. doi: 10.5006/3134.

[49] J. Srinivasan and R. G. Kelly, "On a Recent Quantiative Framework Examining the Critical Factors for Localized Corrosion and Its Impact on the Galvele Pit Stability Criterion," *Corrosion,* vol. 73, pp. 613-633, 2017. doi: 10.5006/2334.

[50] P. C. Pistorius and G. T. Burstein, "Metastable Pitting Corrosion of Stainless Steel and the Transition to Stability," *Philosophical Transactions of the Royal Society A,* vol. 341, pp. 531-559, 1992. doi: 10.1098/rsta.1992.0114.

[51] G. T. Gaudet, W. T. Mo, T. A. Hatton, J. W. Tester, J. Tilly, H. S. Isaacs and R. C. Newman, "Mass Transfer and Electrochemical Kinetic Interactions in Localize Pitting Corrosion," *American Institute of Chemical Engineers Journal,* vol. 32, pp. 949-958, June 1986. doi: 10.1002/aic.690320605.

[52] P. Ernst and R. C. Newman, "Pit Growth Studies in Stainless Steel Foils. I. Introduction and Pit Growth Kinetics," *Corrosion Science,* vol. 44, no. 5, pp. 927-941, May 2002. doi: 10.1016/S0010-938X(01)00133-0.

[53] J. Jun, G. S. Frankel and N. Sridhar, "Effect of Chloride Concentration and Temperature on Growth of 1D Pit," *Journal of Solid State Electrochemistry,* vol. 19, pp. 3439-3447, February 2015. doi:10.1007/s10008-015-2780-4.

[54] A. Kosaki, "Evaluation Method of Corrosion Lifetime of Conventional Stainless Steel Canister Under Oceanic Air Environment," *Nuclear Engineering and Design,* vol. 238, no. 2008, pp. 1233-1240, 2008. doi: 10.1016/j.nucengdes.2007.03.040.

[55] T. Nakayama and M. Takano, "Application of a Slip Dissolution-Repassivation Model for Stress Corrosion Cracking of AlSl 304 Stainless Steel in a Boiling 42% MgCl2 Solution," *Corrosion,* vol. 42, no. 1, pp. 10-15, 1986. doi: 10.5006/1.3584873.

[56] D. Spencer, M. Edwards, M. Wenman, C. Tsitsios, G. Scatigno and R. Chard-Tuckey, "The Initiation and Propagation of Chloride-Induced Transgranular Stress-Corrosion Cracking (TGSCC) of 304L Austenitic Stainless Steel Under Atmospheric Conditions," *Corrosion Science,* vol. 88, pp. 76-88, 2014. doi: 10.1016/j.corsci.2014.07.017.

[57] G. D. P. Scatigno, M. Ryan and M. Wenman, "The Effect of Salt Loading on Chloride-Induced Stress Corrosion Cracking of Austenitic Stainless Steel Under Atmospheric Conditions," *Materialia,* vol. 8, p. Article 100509, 2019.

[58] M. Yajima and M. Arii, "Chloride Stress-Corrosion Cracking of AISI-304 Stainless Steel in Air," *Materials Performance,* vol. 19, no. 12, pp. 17-19, 1980.

[59] S. Shoji and N. Ohnaka, "Effects of Relative Humidity and Chloride Type on Stainless-Steel Room-Temperature Atmospheric Corrosion Cracking," *Corrosion Engineering,* vol. 38, pp. 111-119, 1989. doi: 10.1016/j.mtla.2019.100509.

[60] C. Örnek and D. Engelberg, "Toward Understanding the Effects of Strain and Chloride Deposition Density on Atmospheric Chloride-Induced Stress Corrosion Crack of Type 304 Austenitic Stainless Steel Under MgCl2 and FeCl3:MgCl2 Droplets," *Corrosion,* vol. 75, no. 2, pp. 167-182, 2019.

[61] H. Hayashibara, M. Mayuzumi, Y. Mizutani and J. Tani, "Effect of Temperature and Humidity on Atmospheric Stress Corrosion Cracking of Stainless Steel," in *Proceedings of the 2008 NACE Corrosion Conference*, New Orleans LA, March 2008.

[62] N. Fairweather, N. Platts and D. Tice, "Stress-Corrosion Crack Initiation of Type 304 Stainless-Steel in Atmospheric Environments Containing Chloride: Influence of Surface Condition, Relative Humidity, Temperature and Thermal Sensitization," in *NACE International Corrosion Conference and Expo*, New Orleans LA, 2008.

[63] A. Cook, N. Stevens, J. Duff, A. Mishelia, T. S. Leung, S. Lyon, J. Marrow, W. Ganther and I. Cole, "Atmospheric-Induced Stress Corrosion Cracking of Austenitic Stainless Steels Under Limited Chloride Supply," in *Proceedings of the 18th International Corrosion Conference*, November 2011.

[64] G. Nakayama and Y. Sakakibara, "Prediction Model for Atmospheric Stress Corrosion Cracking of Stainless Steel," *The Electrochemical Society Transactions,* vol. 50, no. 31, p. 303, 2013. 10.1149/05031.0303ecst.

[65] K. Shirai, T. Saegusa and J. Tani, "Study on Interim Storage of Spent Nuclear Fuel by Concrete Cask for Practical Use. Feasibility Study on Prevention of Chloride Induced Stress Corrosion Cracking for 304L Stainless Steel Canister (English translation)," *Denryoku Chuo Kenkyusho Hokoku,* vol. 43, no. 30, pp. 1-4, 1-18, 2011.

[66] D. S. Dunn, "NRC Perspective on Information Needs for CISCC of Spent Fuel Dry Storage Systems," in *DOE UFD Stress Corrosion Cracking Workshop*, Las Vegas NV, September 2015.

[67] M. O. Speidel, "Stress Corrosion Cracking of Stainless Steels," *Metallurgical Transactions A,* vol. 12, pp. 779-789, May 1981. doi: 10.1007/BF02648342.

[68] L. Tjayadi, N. Kumar and K. L. Murty, "Accelerated Crack Growth Experiments of SS304H for Dry Storage Canister in Substitute Ocean Water - Effect of Temperature," *Materials Today Communications,* vol. 23, no. 2020, p. 100929, 2020. doi: 10.1016/j.mtcomm.2020.100929.

[69] P. Lam, A. J. Duncan and R. L. Sindelar, "Crack Growth Rate and Large Plate Demonstration of Chloride-Induced Stress Corrosion Cracking in Spent Nuclear Fuel Storage Canisters," SRNL-STI-2019-00561, Savannah River National Laboratory, Jackson SC, September 2019.

[70] H. Shaikh, H. Khatak and P. Rodriguez, "Stress Corrosion Crack Growth Behavior of Austenitic Stainless Steels in Hot Concentrated Chloride Solution," in *Proceedings of the 10th International Conference on Fracture*, Honolulu HI, 2001..

[71] P. Dong, G. G. Scatigno and M. R. Wenman, "Effect of Salt Composition and Microstructure on Stress Corrosion Cracking of 316L Austenitic Stainless Steel for Dry Storage Casks," *Journal of Nuclear Materials,* vol. 545, no. 2021, p. 152572, 2021. doi: 10.1016/j.jnucmat.2020.152572.

[72] J. I. Tani, M. Mayuzumi and N. Hara, "Initiation and Propagation of Stress Corrosion Cracking of Stainless Steel Canister for Concrete Cask Storage of Spent Nuclear Fuel," *Corrosion,* vol. 65, no. 3, pp. 187-194, 2009. doi: 10.5006/1.3319127.

[73] O. E. Albores-Silva, E. A. Charles and C. Padovani, "Effect of Chloride Deposition on Stress Corrosion Cracking of 316L Stainless Steel Used for Intermediate Level Radioactive Waste Containers," *Corrosion Engineering, Science, and Technology,* vol. 46, no. 2, pp. 124-128, April 2011. doi: 10.1179/1743278210Y.0000000004.

[74] H. P. Hawkes, F. H. Beck and M. G. Fontana, "Effect of Applied Stress and Cold Work on Stress Corrosion Cracking of Austenitic Stainless Steel by Boiling 42 Percent Magnesium Chloride," *Corrosion,* vol. 19, no. 7, pp. 247t-253t, 1963. doi: 10.5006/0010-9312-19.7.247.

[75] A. J. Russell and D. Tromans, "A Fracture Mechanics Study of Stress Corrosion Cracking of Type-316 Austenitic Steel," *Metallurgical Transactions A,* vol. 10, pp. 1229-1238, 1979. doi: 10.1007/BF02811978.

[76] C. Paige, "Computer Solution and Perturbation Analysis of Generalized Linear Least Squares Problems," *Mathematics of Computation,* vol. 33, no. 145, pp. 171-183, 1979.

[77] C. Goodall, "Computation Using the QR Decomposition," *Computational Statistics,* Vols. Vol 9 of Handbook of Statistic, edited by C.R. Rao, North Holland, pp. 492-494, 1993.

[78] H. Khatak, J. Ghanamoorthy and P. Rodriguez, "Studies on the Influence of Metallurgical Variables on the Stress Corrosion Behavior of AISI 304 Stainless Steel in Sodium Chloride Solution Using the Fracture Mechanics Approach," *Metallurgical and Materials Transactions A,* vol. 27, pp. 1313-1325, 1996.

[79] M. Louthan, J. Derrick and R. Derrick, "Hydrogen Transport in Authenitic Stainless Steel," *Corrosion Science,* vol. 15, pp. 556-577, 1975.

[80] J. K. Kruschke, Doing Bayesian Data Analysis: A Tutorial with R, JAGS, and Stan, Elsevier Inc., 2015.

[81] M. Plummer, *JAGS: Just Another Gibbs Sampler,* 2012.

[82] G. Casella and R. L. Berger, Statistical Inference, Pacific Grove CA: Duxbury, 2002.

[83] H. S. Isaacs and R. C. Newman, *American Institute of Chemical Engineers Journal,* vol. 32, pp. 949-958, 1986.